Chapter 4

Barrier Distributions from Elastic Scattering

4.1 Theoretical Considerations

The barrier distribution representations $D^{qel}(E)$ discussed in the last chapter show a reduction of sensitivity to the barrier structure at the higher energies. This appears to be due to the de-phasing of the various scattering amplitudes which contribute to the quasi-elastic scattering cross section. The de-phasing is caused by the differences in kinetic energy and orbital angular momentum between the many channels. Such de-phasing can therefore not occur, when only one particular quasi-elastic scattering channel, e.g. the elastic scattering channel, is considered. It is thus of interest to investigate, if it might be possible to develop a barrier distribution representation utilizing elastic scattering excitation functions. Such a possibility may be anticipated, because in the case of transfer reactions it has already been shown in Section 3.2.4 that individual quasi-elastic scattering channels can contain information about the barrier structure.

As in the last chapter, the approach may be based on the sudden and the iso-centrifugal approximations, so that the dynamics of the nuclear binary system can be treated analytically in the eigen-channel model. This description of elastic scattering is similar to that applied by Takigawa *et al.* in the interpretation[1,2] of the experimental angular distributions for elastic scattering of the system ^{18}O + ^{184}W, for which pronounced deviations from the Fresnel diffraction pattern are observed[3]. In the eigen-channel model the elements S_j^ℓ of the scattering matrix for the physical reaction channels j are given by Equation 1.48 as linear superpositions of the elements of the scattering matrix $\bar{S}_k^\ell$ for the eigen-channels ($k = 0, 1, .., n$), i.e.

$$S_j^\ell = U_{jk} U_{0k} \bar{S}_k^\ell \tag{4.1}$$

The unitary matrix $U_{i\alpha}$ diagonalizes the nuclear coupling matrix and the factor $U_{0\alpha}$ accounts for the boundary condition[4] that there is incident flux only in the entrance channel (j=0). The scattering amplitudes $f_j(E, \theta)$ for the physical reaction channels as given by Equation 1.64 can then be expressed as

$$f_j(E,\theta) = \frac{\lambda}{2i} \sum_{\ell,k} (2\ell + 1) P_\ell(\cos\theta) \exp[2i\sigma_k^\ell] U_{jk} U_{0k} \bar{S}_k^\ell \tag{4.2}$$

[1] N.Takigawa *et al.*, Phys. Lett. B **262** (1991) 199.

[2] N.Takigawa *et al.*, Phys. Rev. C **44** (1991) 477.

[3] C.E. Thorn *et al.*, Phys. Rev. Lett. **38** (1977) 384.

[4] M.A. Nagarajan, N. Rowley, R. Lindsay, J. Phys. G: Nucl. Part. Phys. **12** (1986) 529.

where $\lambda\!\!\!^-$ is the asymptotic de Broglie wave length and σ_k^ℓ are the Coulomb phases. Introducing the eigen-channel weights

$$W_k \equiv |U_{0k}|^2; \qquad \sum_{k=0}^{n} W_k = 1 \tag{4.3}$$

the physical elastic scattering amplitude $f^{el} \equiv f_{j=0}$ can be written as

$$f^{el}(E,\theta) = \sum_{k=0}^{n} W_k f_k(E,\theta,B_k) \equiv \sum_{k=0}^{n} W_k |f_k| e^{i\phi_k}. \tag{4.4}$$

where the ϕ_k are the phases of the complex eigen-channel amplitudes $f_k(E,\theta,B_k)$. This coherent sum is similar to the incoherent sum for the fusion cross section (1.51) which contains the same weights W_k.

For elastic scattering from a potential barrier B_k at a fixed angle θ and f^R being the Rutherford scattering amplitude, the function

$$G^{el}(E,B_k) \equiv -\frac{d}{dE}|f_k/f^R| \tag{4.5}$$

defines a peaked function similar to the functions $G^{fus}(E,B_k), G^{qel}(E,B_k)$ and $G^{trans}(E,B_k)$ introduced earlier. As is the case for $G^{qel}(E,B_k)$, the function $G_k^{el}(E)$ for $\theta = 180°$ is centred at $E_{cm} = B_k$, whereas for $\theta < 180°$ it is shifted by the centrifugal energy which can be corrected for using Equation 3.16.

The function $G^{el}(E,B_k)$ at 180° as derived from a single barrier optical model calculation is compared with $G^{fus}(E,B_k)$ in Figure 4.1(a). The comparison shows that the function $G^{el}(E,B_k)$ is representative of the barrier B_k, but about 20% wider than $G^{fus}(E,B_k)$.

If the phases $\phi_k(E)$ do not depend too strongly on the eigen-channels k, i.e. $\phi_k(E) \approx \phi_{k'}(E)$, differentiation of the modulus of Equation 4.4 with respect to energy gives for a fixed angle θ

$$-\frac{d}{dE}\left|\frac{f^{el}}{f^R}\right| = -\frac{d}{dE}\left[\frac{d\sigma^{el}}{d\sigma^R}(E)\right]^{1/2} = -\frac{d}{dE}\sum_{k=0}^{n} W_k \left|\frac{f_k}{f^R}e^{i\phi_k}\right| \approx \sum_{k=0}^{n} W_k G^{el}(E,B_k) \tag{4.6}$$

The distribution

$$D^{el}(E) \equiv -\frac{d}{dE}\left[\frac{d\sigma^{el}}{d\sigma^R}(E)\right]^{1/2} \tag{4.7}$$

then represents the weights and heights of the barriers B_k. The accuracy of this representation depends, however, crucially on the assumption that differences between

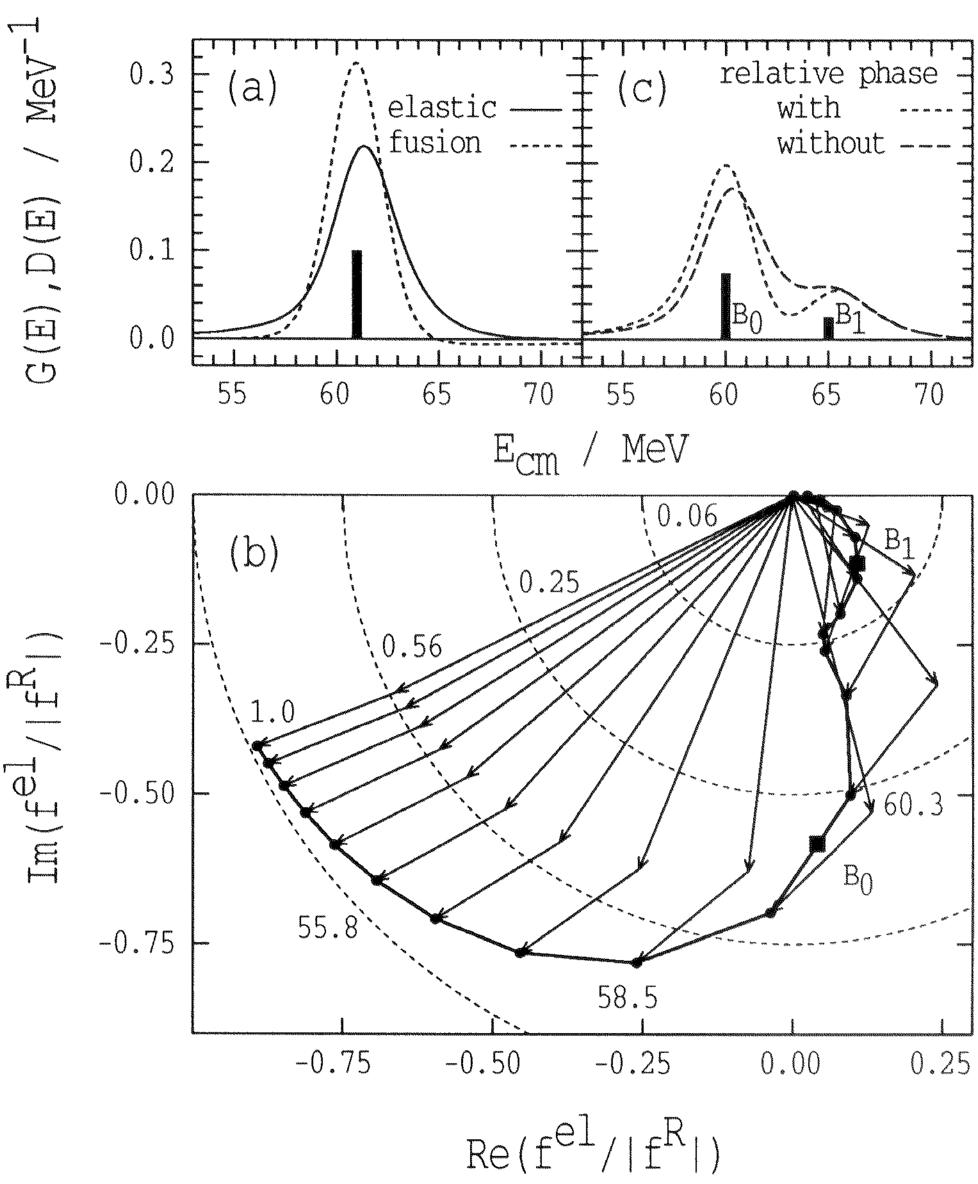

Figure 4.1: *(a) The single barrier functions $G^{el}(E, B_k)$ and $G^{fus}(E, B_k)$. (b) The elastic amplitude for scattering from two barriers $B_{k=0}$ and $B_{k=1}$ plotted in the complex plane. The vectors represent the two components of the amplitude and the filled circles their sum. The calculations have been performed at intervals of 0.9 MeV. Certain energies are indicated, as are the barrier heights (squares). The dashed curves correspond to fixed ratios σ^{el}/σ^R, as given. (c) The distribution $D^{el}(E)$ as extracted from panel (b) by adding the two components with and without the relative phase. The solid bars represent the barrier heights and weights.*

the phases ϕ_k of the various complex eigen-channel amplitudes $f_k(E)$ are small. It is therefore important to investigate the possible effects of phase differences between the eigen-channel amplitudes.

To do this one may consider the two eigen-barriers which reproduce $D^{fus}(E)$ for ^{16}O + ^{144}Sm within the eigen-channel model, as extracted from the fusion data in Section 3.2.3. The best fit to $D^{fus}(E)$ is shown in Figure 4.3(a). The parameters of the two barriers are given in Table 4.1. For each of the two barriers an optical-model calculation was carried out to determine the elastic scattering excitation function at 170°. The potentials used were identical except for the radius parameter of the real part which was adjusted to reproduce the two barrier heights. The imaginary potential was totally absorbing and confined to the nuclear interior. Figure 4.1(b) shows, in the complex plane, the quantities $f_{k=0,1}/|f^R|$, along with their sum $f^{el}/|f^R|$, for various values of E_{cm}. The short-dashed curve in Figure 4.1(c) shows the corresponding distribution $D^{el}(E)$ (4.7), obtained with the correct phase differences $[\phi_{k=0}(E) - \phi_{k=1}(E)]$ between the two scattering amplitudes. The long-dashed curve in Figure 4.1(c) shows $D^{el}(E)$ with this phase difference set to zero for all energies.

Ignoring the relative phase, the sensitivity of $D^{el}(E)$ is limited only by the width of $G_k^{el}(E, B_k)$. Despite the larger width of this function, when compared to the equivalent one for fusion, both distributions $D^{el}(E)$ in Figure 4.1(c) reveal the two barriers. The inclusion of the phase difference between the eigen-channel scattering amplitudes is seen to enhance the sensitivity of $D^{el}(E)$ to the barrier structure and compensates for the 20% increase in width of $G_k^{el}(E, B_k)$ compared to $G_k^{fus}(E, B_k)$. This suggests that the barrier structure might be just as easily revealed by its elastic scattering representation $D^{el}(E)$ as by the distribution $D^{fus}(E)$ from fusion data.

4.2 Experimental Tests of the Method

4.2.1 The Systems ^{16}O + ^{144,154}Sm, ^{186}W and ^{208}Pb

The distributions $D^{el}(E)$ have been tested utilizing the elastic scattering excitation functions which have been measured at $\theta_{lab} = 170°$ for the systems ^{16}O + ^{144}Sm, ^{154}Sm, ^{186}W and ^{208}Pb as described in Section 2.4. These excitation functions are shown in Figures 3.3, 3.4 and 3.12 and they are tabulated in Tables A.5– A.8 in the Appendix. The data have been transformed into the distributions $D^{el}(E)$ using the point-difference formula

$$D^{el}(E) = -\frac{\sqrt{d\sigma^{el}/d\sigma^{R}(E+0.5\Delta E)} - \sqrt{d\sigma^{el}/d\sigma^{R}(E-0.5\Delta E)}}{\Delta E} \tag{4.8}$$

with an energy step $\Delta E_{lab} = 2$ MeV. The experimental distributions $D^{el}(E)$ are compared with the corresponding distributions $D^{fus}(E)$ from fusion[5,6] in Figure 4.2. To facilitate the comparison the fusion data have been divided by the classical cross section πR_0^2, where R_0 is the average barrier radius, so that the area under the distribution is unity within the experimental uncertainty, as it is for $D^{el}(E)$ by definition.

The systems ^{16}O + ^{154}Sm and ^{16}O + ^{186}W both have wide barrier distributions due to the large prolate deformations of the targets. However, the weighting of the barriers is very different for the two systems. This can be seen in the representations $D^{fus}(E)$ in Figs. 2a,b and has been shown[7] to be due to the opposite signs of the hexadecapole moments of ^{154}Sm and ^{186}W. For the tungsten target $D^{fus}(E)$ rises much more steeply at low energies, whereas for the samarium target, the data peak at high energies and do not show the plateau evident in the tungsten data. The distributions $D^{el}(E)$ reflect the same features but are somewhat wider, possibly due to the larger width of the function $G^{el}(E, B_k)$.

A similar qualitative agreement also exists for the other two reactions, ^{16}O + ^{144}Sm and ^{16}O + ^{208}Pb, shown in Figure 4.2(c,d). For ^{16}O+^{144}Sm, $D^{fus}(E)$ displays two distinct peaks. Contrary to the expectations from the theoretical considerations in Section 4.1 the higher-energy peak is absent from $D^{el}(E)$ which merely shows a smooth tail instead.

4.2.2 Detailed Analysis of ^{16}O+^{144}Sm

The experimental results for the system ^{16}O+^{144}Sm have been studied in more detail within the eigen-channel model. The distribution $D^{el}(E)$ has been fitted with Equation 3.18 in the same way as has been discussed in Section 3.2.3 for the distributions $D^{fus,qel}(E)$. The best fit to $D^{el}(E)$ is shown in Figure 4.3(b) and its parameters are given in Table 4.1. The two barriers extracted from $D^{el}(E)$ agree within experimental uncertainty in height and weight with the ones extracted

[5] J.R. Leigh *et al.*, Phys. Rev. C **52** (1995) 3151.

[6] C.R. Morton *et al.*, Phys. Rev. C **52** (1995) 243.

[7] R.C. Lemmon *et al.*, Phys. Lett. B **316** (1993) 32.

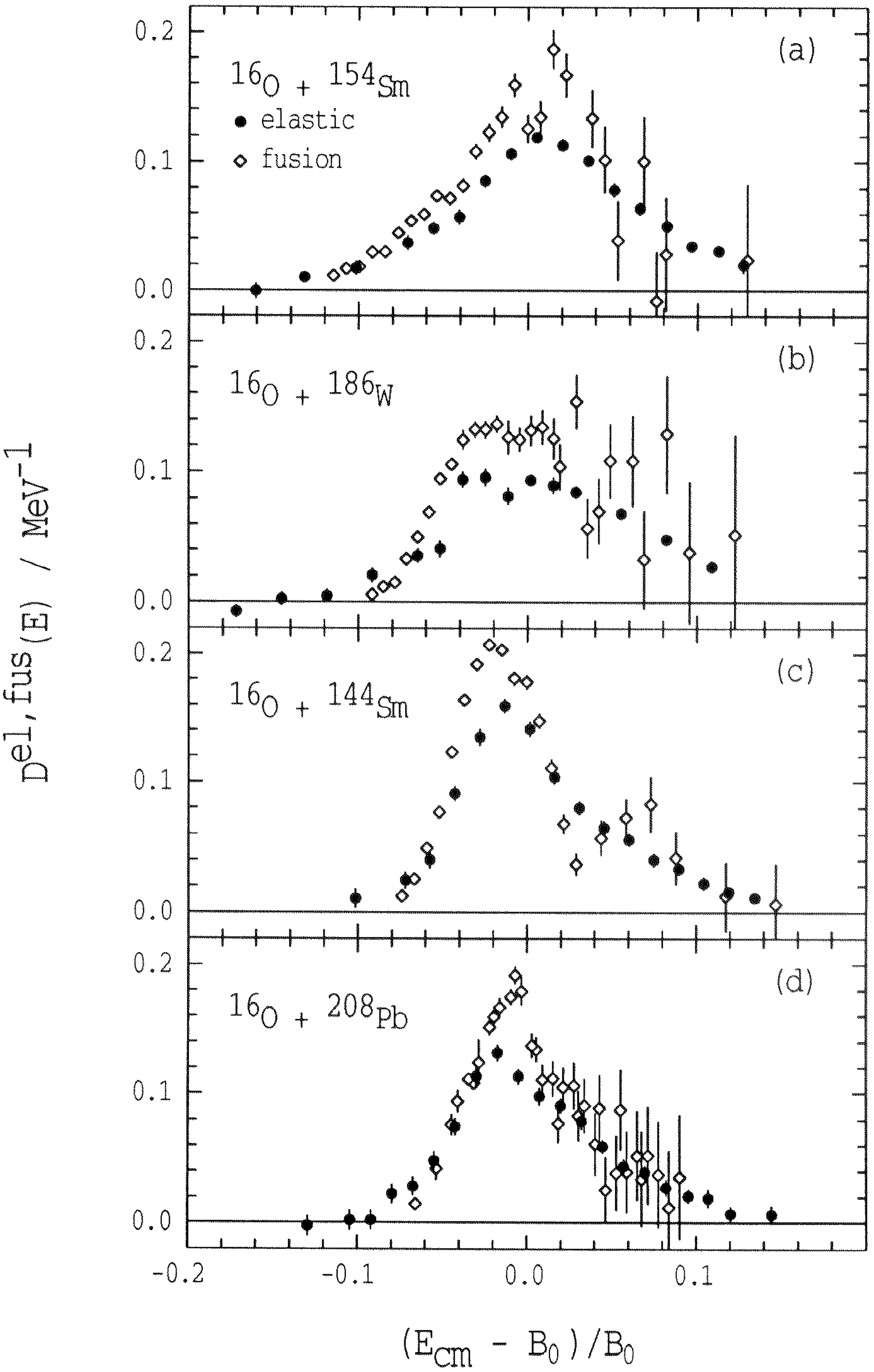

Figure 4.2: *The experimental representations $D^{el}(E)$ and $D^{fus}(E)$ of the barrier distributions for the systems indicated. The energy axis is represented by $(E - B_0)/B_0$, where B_0 is the appropriate average barrier height.*

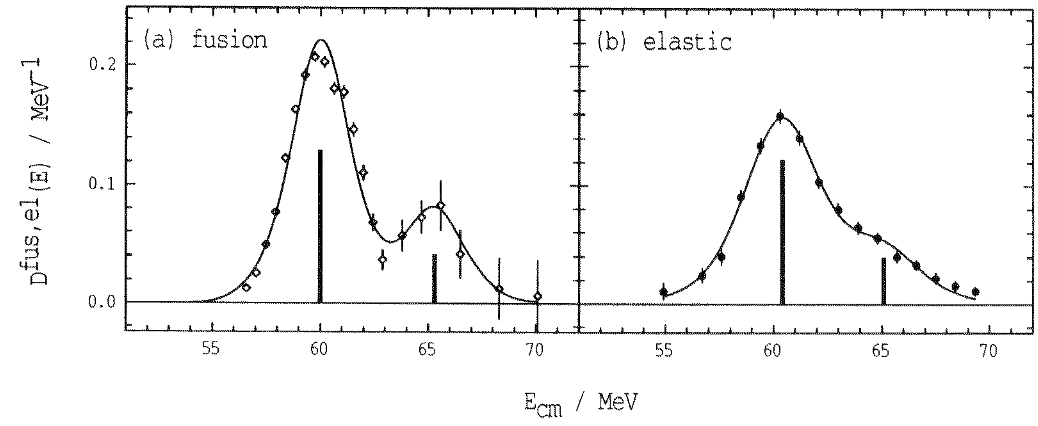

Figure 4.3: *Two-barrier fits to (a) $D^{fus}(E)$ and (b) $D^{el}(E)$ for ^{16}O + ^{144}Sm. The barrier heights B_k and relative weights W_k are indicated by the bars.*

from $D^{fus}(E)$. A distortion of the distribution $D^{el}(E)$ similar to that observed for $D^{qel}(E)$ is not present. The fits to $D^{fus}(E)$ and $D^{el}(E)$ disagree, however, in the peak width ΔB. Similar to $D^{qel}(E)$ the width of a single peak in the distribution $D^{el}(E)$ is larger (~20%) than in $D^{fus}(E)$. This reduces the sensitivity of $D^{el}(E)$ to the barrier structure. The phase effect predicted from the calculations shown in Figure 4.1(b,c), which was expected to compensate for the larger width and increase the sensitivity, does not appear to occur.

In order to understand this result, exact coupled-channels calculations have been performed for $^{16}O+^{144}Sm$. These calculations employed the code ECIS[8] and used the Woods-Saxon parameters $V_0 = 162$ MeV, $r_0 = 1.0$ fm, $a_0 = 0.9$ fm, $W_0 = 30.0$ MeV, $r_w = 1.0$ fm and $a_w = 0.4$ fm. They considered vibrational couplings to states of ^{144}Sm. The lowest 2^+ state at 1660 keV and the lowest 3^- state at 1810 keV were included in the calculations. The coupling strengths were derived from B(Eλ)-values[9,10] with Equation 3.20 and $R_a = 1.06A^{1/3}$ fm, but increased arbitrarily by 20% to yield the deformation parameters $\beta_2 = 0.14$ and $\beta_3 = 0.25$. The 20% increase results in a better reproduction of the fusion data. Apart from this modification the ECIS-calculations are identical to the ones discussed in Section 3.2.3. The fusion cross section was taken to be the total reaction cross section minus the cross

[8] J. Raynal, Computing as a Language of Physics, I.A.E.A Vienna (1972) 281.

[9] J.K. Tuli, Nucl. Data Sheets **56** (1989) 683.

[10] R. Spear, At. Data Nucl. Data Tables **42** (1989) 55.

	$^{16}O + ^{144}Sm$			
	fusion		elastic	
k	B_k / MeV	W_k	B_k / MeV	W_k
0	60.0 ± 0.2	0.80 ± 0.03	60.4 ± 0.2	0.73 ± 0.04
1	65.3 ± 0.3	0.26 ± 0.09	65.1 ± 0.3	0.20 ± 0.04
ΔB / MeV	3.2 ± 0.2		4.1 ± 0.3	

Table 4.1: *The heights B_k and weights W_k of the potential barriers present in the reaction ^{16}O + ^{144}Sm as extracted from two-barrier fits to the experimental distributions $D^{fus,el}(E)$. The last line gives the width ΔB of a single peak in the distribution.*

sections for the 2^+ and 3^- reaction channels. It can be seen from Figure 4.4(a) that these calculations reproduce well the structure of $D^{fus}(E)$. Up to the average fusion barrier, the calculation for $D^{el}(E)$ is also in good agreement with the data. However, it fails at the higher energies where it predicts a second peak. Since ECIS treats the phases of the scattering amplitudes properly, this discrepancy cannot be due to the phase approximation which has been used in the derivation of $D^{el}(E)$. It must have some other origin.

Pronounced structures of elastic scattering excitation functions have been discussed theoretically by other authors[11]. They found that the extension of the volume imaginary potential into the barrier region to simulate direct-reaction channels not explicitly included in the coupling matrix smears out the structure in the excitation function. Such residual channels account for a large part of the reflected flux at energies above the average barrier as has been pointed out in Section 3.2.3. Following these findings the coupled-channels calculations have been repeated with the inclusion of a surface imaginary potential with $W_s = 4$ MeV, $r_s = 1.22$ fm, $a_s = 0.43$ fm. This surface potential, which is shown in Figure 4.4(c), is centred inside the barrier but is non-zero at the barrier radius. The solid curve in Figure 4.4(b) shows the predicted distribution $D^{el}(E)$ which now follows closely the experimental data.

Figure 4.4(b) also shows two eigen-channel calculations, which are analogous to those of Figure 4.1(c), but in addition contain the surface absorptive potential. The long-dashed curve ignores the relative phase and leads to a distribution which is smoother than the equivalent curve in Figure 4.1(c). The reason for this may be seen

[11] A.T. Kruppa *et al.*, Nucl. Phys. A **560** (1993) 845.

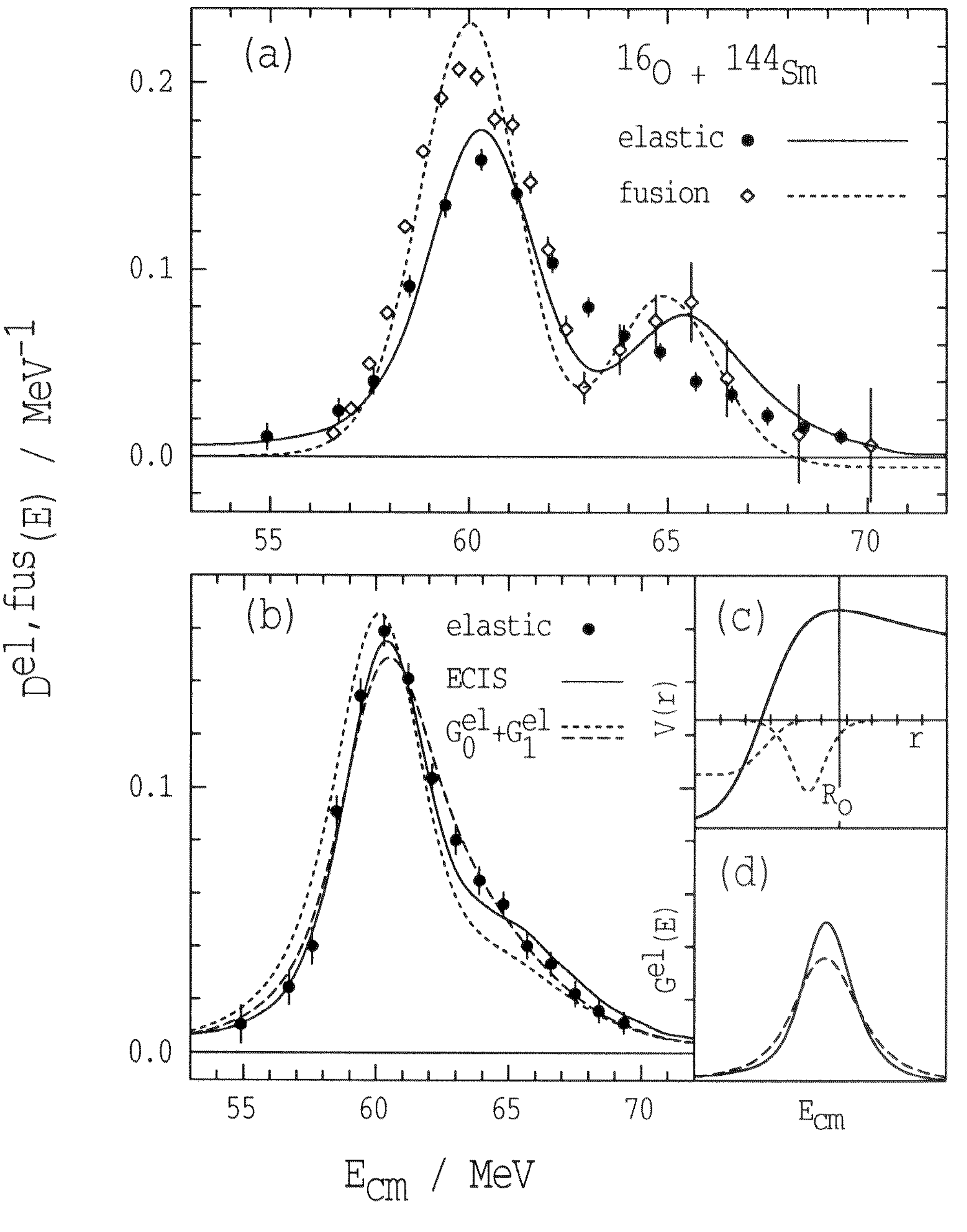

Figure 4.4: *(a) The experimental distributions $D^{el}(E)$ and $D^{fus}(E)$ for ^{16}O + ^{144}Sm are compared with exact coupled-channels calculations. (b) The same calculations for $D^{el}(E)$ with the inclusion of surface absorption. Superpositions of the two broadened functions $G^{el}(E, B_k)$ (labelled as G_k^{el}) for $B_{0,1}$= 60 and 65 MeV are also shown both without (long-dashed curve) and with (short-dashed curve) the relative phase. (c) The real (solid curve) and imaginary (dashed curves) potentials in the barrier region. The surface imaginary potential has been multiplied by 10. (d) $G^{el}(E, B_k)$ with (long-dashed curve) and without (solid curve) surface absorption.*

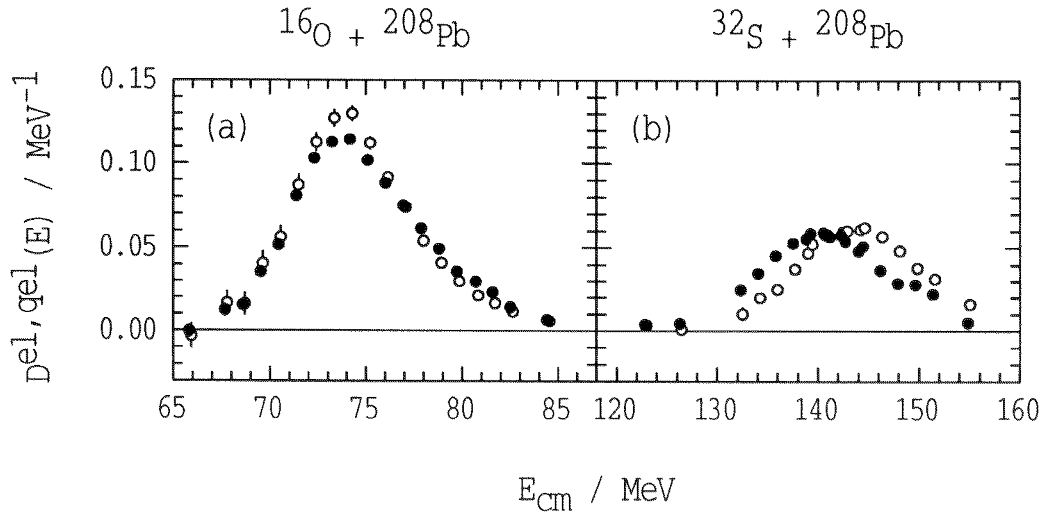

Figure 4.5: *The distributions $D^{qel}(E)$ and $D^{el}(E)$ (a) $^{16}O + ^{208}Pb$ and (b) $^{32}S + ^{208}Pb$. They have been extracted using an energy step $\Delta E_{lab} = 4MeV$ in the point-difference formula. For both distributions the energies have been reduced by the centrifugal energy.*

from Figure 4.4(d), which shows that the underlying function $G^{el}(E, B_k)$ is further widened by the inclusion of surface absorption. In the calculations in Figure 4.1(c), the relative phase enhances the barrier structure. The corresponding calculations with surface absorption are shown in Figure 4.4(b). The calculation including the phase relations is displayed as short-dashed curve. It is different from the eigen-channel calculation shown as long-dashed curve, but it does not resolve the two-peak structure. It thus appears that the presence of the residual channels broadens the function $G^{el}(E, B_k)$, so that the sensitivity of the representation $D^{el}(E)$ to the barrier distribution is reduced, when compared with $D^{fus}(E)$.

It should be noted that within the optical model it is not possible to distinguish flux absorbed by the surface imaginary potential from flux absorbed by the volume imaginary potential. Thus the effect of surface absorption on $D^{fus}(E)$ cannot be deduced from this calculation. The effects of the residual channels on fusion may, however, be studied in more detail with coupled-channels calculations which utilize the in-going wave boundary condition.

4.2.3 The System ^{32}S + ^{208}Pb

Using the measured elastic scattering excitation function displayed in Figure 3.12(b) the distribution $D^{el}(E)$ has also been extracted for the system ^{32}S + ^{208}Pb using an energy step $\Delta E_{lab} = 4$ MeV in Equation 4.8. It is shown in Figure 4.5 together with the distribution $D^{qel}(E)$ for this system extracted with the same energy step and the two corresponding distributions for the system ^{16}O + ^{208}Pb. The relatively large energy step used in the point-difference formulae results in well defined distributions. For both systems the two independent representations of the barrier distribution are consistent with each other. While they do not resolve individual barriers the representations reflect the differences between the two barrier distributions. The centroids of the distributions may be associated with an average potential barrier. The centroids of $D^{qel}(E)$ and $D^{el}(E)$ for ^{16}O + ^{208}Pb are essentially identical. This is also the case for the other oxygen reactions studied in this work. In contrast the centroids of $D^{qel}(E)$ and $D^{el}(E)$ for ^{32}S + ^{208}Pb differ. The distribution $D^{el}(E)$ is shifted downwards in energy by nearly 4 MeV, whereas, as for the other systems, $D^{qel}(E)$ overlaps with $D^{fus}(E)$, as has been shown in Figure 3.14.

The question arises, if the energy shift of $D^{el}(E)$ has any physical significance. The system ^{32}S + ^{208}Pb is the heaviest one studied in this work. It has the effective fissility $x_e = 0.56$. This compares with $x_e = 0.38$ for ^{16}O + ^{208}Pb. The sulphur reaction is thus intermediate between light systems and heavy systems for which 'extra push' has been observed, as shown in Figure 1.14. It has been demonstrated in the previous sections that for lighter systems the distribution $D^{el}(E)$ is representative of the barrier distribution. If this is also true for heavier systems such as ^{32}S + ^{208}Pb, it may be argued that $D^{el}(E)$ represents the 'true' potential barriers, since elastic scattering by definition cannot be subject to dissipation effects. In contrast, fusion, inelastic scattering and transfer reactions are processes during which dissipation can occur. Consequently, the barrier distribution representations $D^{fus}(E)$ and $D^{qel}(E)$ may include the effects of dissipation. It is interesting to note that, as shown by Figure 3.12, in the system ^{32}S + ^{208}Pb the contribution of inelastic and transfer channels to the quasi-elastic scattering cross section is significantly larger than in the oxygen reactions studied in this work. This in itself is an indication of increased dissipation.

If the approximations implicit in their derivations are reasonably good for heavier systems, the novel representations of elastic and quasi-elastic scattering data developed in this thesis might thus offer the possibility to study the 'extra push' phenomenon, without invoking the classical Bass model as a reference. The fusion hindrance may e.g. be defined as the energy difference between the centroids of $D^{el}(E)$ and $D^{fus}(E)$. If it is found that the overlap between $D^{qel}(E)$ and $D^{fus}(E)$ persists for heavy systems, the predictions of the macroscopic fusion models, like the surface-friction model, may then be tested without performing complicated fusion measurements, but by simply comparing the centroids of $D^{el}(E)$ and $D^{qel}(E)$ as measured at backward angles. A critical factor in such an approach will be the importance of deep-inelastic reaction channels. These very dissipative reactions which occur in heavy systems are not accounted for in the derivation of the distribution $D^{qel}(E)$, so that the simple interpretation of $D^{qel}(E)$ as a barrier distribution representation may be lost. However, it may be hoped, that at least for intermediate systems 'extra push' energies can be determined in this way.

4.3 Concluding Remarks

The function $D^{el}(E)$ which has been derived in this chapter within the eigen-channel model is representative of the barrier distribution of a reaction. The observed structures in the experimental distributions $D^{el}(E)$ are therefore direct evidence for the effects of channel-coupling on the elastic scattering channel.

In contrast to the distribution $D^{qel}(E)$, $D^{el}(E)$ is not affected by the iso-centrifugal and sudden approximations, since for elastic scattering there is no change in angular momentum and energy during the collision. Thus there cannot be distortions of $D^{el}(E)$ at the higher energies as observed for $D^{qel}(E)$ due to the de-phasing of scattering amplitudes. The derivation of $D^{el}(E)$ relies, however, on the assumption that the phase differences between scattering from different eigen-channel barriers are small and approximately constant with energy. This assumption is generally not valid, but large changes of the phase differences occur typically when the centre-of-mass energy is close to the height of a barrier and can thus result in an enhancement of the structure in $D^{el}(E)$. The sensitivity of the experimental distributions $D^{el}(E)$ to the barrier structure is, however, reduced compared to that of $D^{fus}(E)$. This is due to the larger width of a single peak in $D^{el}(E)$ when compared to a single peak in $D^{fus}(E)$. This broadening, similarly to the distortion effect in $D^{qel}(E)$ at the higher energies, has been related to the presence of the residual channels, which are not explicitly included in the coupled-channels calculations. The presence of these residual channels, which are dominantly transfer reactions, appear to widen the function $G^{el}(E, B_k)$.

The technique to extract the barrier distribution of a system from elastic scattering as presented in this chapter is best suited for reactions with well separated potential barriers. Such a situation may be expected for systems with single phonon coupling and large products of charges Z_pZ_t. The reaction ^{40}Ca + ^{144}Sm might prove to be such a system. For heavy reactions with fissilities $x_e \gtrsim 0.5$ the comparison of the distribution $D^{el}(E)$ with $D^{fus}(E)$ and $D^{qel}(E)$ might reveal new insights into the effects of dissipation in the collisions of heavy nuclei. For heavy reactions where deep-inelastic channels are not too strong, the centroids of $D^{el}(E)$, $D^{qel}(E)$ and $D^{fus}(E)$, may be associated with average potential barriers. In the case of $D^{el}(E)$ this average barrier should correspond to the true potential barrier, whereas for the other two distributions the centroid might be shifted because of energy dissipation.